Article

Structural Tuning of Charge, Orbital, and Spin Ordering in Double-Cell Perovskite Series between NdBaFeO and HoBaFeO

Patrick M. Woodward, Emmanuelle Suard, and Pavel Karen

J. Am. Chem. Soc., **2003**, 125 (29), 8889-8899• DOI: 10.1021/ja034813+ • Publication Date (Web): 01 July 2003

J|A|C|S
ARTICLES
Published on Web 07/01/2003

Structural Tuning of Charge, Orbital, and Spin Ordering in Double-Cell Perovskite Series between $NdBaFe_2O_5$ and $HoBaFe_2O_5$

Patrick M. Woodward, Emmanuelle Suard, and Pavel Karen*

Contribution from the Department of Chemistry, Ohio State University, 100 West 18th Avenue, Columbus, Ohio 43210-1185, Institute Max von Laue and Paul Langevin, BP156, 38042 Grenoble, France, and Department of Chemistry, University of Oslo, POB1033 Blindern, N-0315 Oslo, Norway

Received February 22, 2003; E-mail: pavel.karen@kjemi.uio.no

Abstract: Charge, orbital, and magnetic ordering of $NdBaFe_2O_5$ and $HoBaFe_2O_5$, the two end-members of the double-cell perovskite series $RBaFe_2O_5$, have been characterized over the temperature range 2−450 K, using differential scanning calorimetry, neutron thermodiffractometry and high-resolution neutron powder diffraction. Upon cooling, both compounds transform from a class-III mixed valence (MV) compound, where all iron atoms exist as equivalent MV $Fe^{2.5+}$ ions, through a "premonitory" charge ordering into a class-II MV compound, and finally to a class-I MV phase at low-temperature. The latter phase is characterized by Fe^{2+}/Fe^{3+} charge ordering as well as orbital ordering of the doubly occupied Fe^{2+} d_{xz} orbitals. The relative simplicity of the crystal and magnetic structure of the low-temperature charge-ordered state provide an unusual opportunity to fully characterize the classical Verwey transition, first observed in magnetite, Fe_3O_4. Despite isotypism of the title compounds at high temperature, neutron diffraction analysis reveals striking differences in their phase transitions. In $HoBaFe_2O_5$, the Verwey transition is accompanied by a reversal of the direct Fe−Fe magnetic coupling across the rare earth layer, from ferromagnetic in the class-II and -III MV phases to antiferromagnetic in the low-temperature class-I MV phase. In $NdBaFe_2O_5$, the larger Nd^{3+} ion increases the Fe−Fe distance, thereby weakening the Fe−Fe magnetic interaction. This decouples the charge and magnetic ordering so that the Fe−Fe interaction remains ferromagnetic to low temperature. Furthermore, the symmetry of the charge-ordered class-I MV phase is reduced from *Pmma* to $P2_1ma$ and the magnitude of the orbital ordering is diminished. These changes destabilize the charge-ordered state and suppress the temperature at which the Verwey transition occurs. A comparison of the magnetic and structural features of $RBaFe_2O_5$ compounds is included in order to illustrate how structural tuning, via changes in the radius of the rare-earth ion, can be used to alter the physical properties of these double-cell perovskites.

Introduction

Electronic, magnetic, and structural phase transitions in mixed-valence (MV) transition-metal oxides have long been a source of extreme interest to chemists and physicists alike. Interesting examples from the literature include long standing phenomena such as the Verwey transition in Fe_3O_4 (magnetite)[1] and charge ordering coupled with a metal−insulator transition in Ti_4O_7 and V_4O_7.[2] More recent examples include charge disproportionation in $YNiO_3$[3] and $CaFeO_3$,[4] charge ordering in the triple perovskite $Ba_3NaRu_2O_9$,[5] and charge, orbital, and magnetic ordering in $NdSrMn_2O_6$.[6,7] It should be noted, however, that recent studies of electronic and magnetic transitions in the latter compound indicate a more complex picture than originally thought, involving charge localization into ferromagnetically coupled dimers rather than isolated Mn^{3+} and Mn^{4+}.[8]

Of particular interest are those compounds where the crystal structure, magnetic ordering and charge ordering are highly correlated. In such cases, competing ground states can be accessed through chemical substitution as well as changes in temperature and/or pressure. The behavior of such compounds provides a direct experimental window on the interrelationships between crystal structure, bonding, electronic band structure and magnetism. Recently, several members of the $RBaFe_2O_5$ family (R = trivalent rare-earth atom) have been shown to undergo phase transitions involving charge, orbital and magnetic ordering.[9,10,11,12] Yet prior to this study the manner in which these phase transitions could be altered via chemical substitution on

(1) Verwey, E. J. W. *Nature (London)* **1939**, *144*, 327.
(2) Marezio, M.; McWhan, D. B.; Dernier, P. D.; Remeika, J. P. *Phys. Rev. Lett.* **1972**, *28*, 1390.
(3) Alonso, J. A.; Martínez-Lope, M. J.; Casais, M. T.; Aranda, M. A. G.; Fernández-Díaz, M. T. *J. Am. Chem. Soc.* **1999**, *121*, 4754.
(4) Woodward, P. M.; Cox, D. E.; Moshopoulou, E.; Sleight, A. W.; Morimoto, S. *Phys. Rev. B* **2000**, *62*, 844.
(5) Stitzer, K. E.; Smith, M. D.; Gemmill, W. R.; zur Loye, H. C. *J. Am. Chem. Soc.* **2002**, *124*, 13 877.
(6) Woodward, P. M.; Cox, D. E.; Vogt, T.; Rao, C. N. R.; Cheetham, A. K. *Chem. Mater.* **1999**, *11*, 3528.
(7) Kuwahara, H.; Tomioka, Y.; Asamitsu, A.; Moritomo, Y.; Tokura, Y. *Science* **1995**, *270*, 961.
(8) Daoud-Aladine, A.; Rodríguez-Carvajal, J.; Pinsard-Gaudart, L.; Fernández-Díaz, M. T.; Revcolevschi, A. *Phys. Rev. Lett.* **2002**, *89*, 097205.

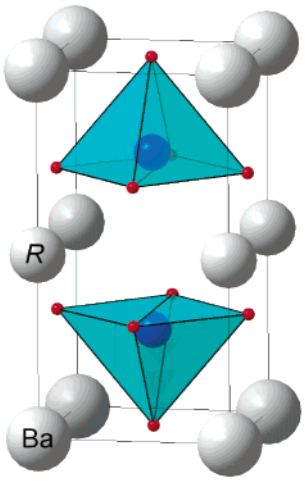

Figure 1. Double-cell perovskite structure of RBaFe$_2$O$_5$.

the seemingly uninvolved R site had not been thoroughly investigated.

The RBaFe$_2$O$_5$ oxides[13] crystallize as double-cell perovskites (Figure 1) analogous to the prototype YBaCuFeO$_5$.[14] Other variants of this structure type include combinations such as Mn and Co,[15] Fe and Co,[15] Co and Cu[16] (but none involving Ni), as well as RBaMn$_2$O$_5$,[17] and RBaCo$_2$O$_5$ [18] phases. The size difference between R^{3+} and Ba^{2+} stabilizes layered ordering of both cations and oxygen vacancies. The latter effect leads to the unusual occurrence of square-pyramidal coordination for iron. At the same time, the RBaFe$_2$O$_5$ stoichiometry bequeaths iron with a half-integer valence. As it is so for several other iron compounds in similar valence situations, a first-order phase transition separates the high-temperature phase in which di- and trivalent iron atoms are not mutually discernible (on the Mössbauer time scale)[9] from the low-temperature phase where charge ordering takes place. The increase in electrical resistivity and molar volume, which accompany the charge disproportionation, as well as the distinct caloric effect, exemplify the classical Verwey transition, first observed in magnetite.[19] However, unlike magnetite where structural details of the charge disproportionation have remained elusive for more than 50 years,[20] the simplicity of double-cell perovskites has enabled researchers to fully characterize the low-temperature crystal and magnetic structures of some representatives, such as TbBaFe$_2$O$_5$ [10] and YBaFe$_2$O$_5$.[12] Therefore, the double-cell perovskites represent an unusually rich library for gaining insight into the details of the discontinuous charge-ordering transitions that are often called Verwey transitions. Another feature that distinguishes the double-cell perovskites from other compounds that undergo charge-ordering transitions is a related transition that precedes the charge ordering proper.[10] Compared with the main Verwey transition, this "premonitory" charge-ordering transition has a weaker thermal effect, produces only a subtle change in electrical conductivity, and thus far, no structural changes have been detected at the premonitory transition. Nonetheless, the possibility remains that careful diffraction studies over a very fine temperature grid would reveal a subtle structural response at this transition. After all, this first attempt to stabilize an ordered arrangement of occupied d orbitals on the iron sublattice appears to be driven by a small magnetostrictive orthorhombic distortion.[9,12]

The peculiarity of the twin nature of charge ordering in these double-cell RBaFe$_2$O$_5$ perovskites coincides interestingly with the Day and Robin classification scheme of the three classes of MV compounds.[21] The high-temperature class-III MV state Fe$^{2.5+}$ (as observed by Mössbauer spectroscopy[10]) separates upon cooling through the temperature T_{PM} of the premonitory transition into two intermediate states Fe$^{2.5+\epsilon}$ and Fe$^{2.5-\epsilon}$ of the class-II MV. Finally, passing through T_V of the main charge-ordering (Verwey) transition produces the integer valence states of iron corresponding to the Day and Robin class-I MV.

Charge-ordering transitions involve a reorganization of the electron density near the Fermi level. Therefore, it is not surprising to find that magnetic interactions play an important role in determining the relative stability of the valence-mixed and charge-ordered states. Antiferromagnetism makes RBaFe$_2$O$_5$ a poorer electrical conductor than magnetite, by many orders of magnitude (cf., refs 11 and 22), although the electrical-conductivity *changes* at Verwey transition are comparable. Ferromagnetic (FM) coupling between the spinel octahedral sites of Fe$^{(tet)}$Fe$^{(oct)}_2$O$_4$ gives a double-exchange related conductivity enhancement that is lacking in RBaFe$_2$O$_5$. Nevertheless, an FM interaction does occur in the latter valence-mixed phase, but only between iron atoms facing each other across the oxygen vacancy in the R layer.[10] As the Fe−Fe distance is dependent upon the radius of the R atom, this provides an opportunity for the R atom to play a role in controlling the charge-ordering transition, perhaps similar to the role that seemingly little involved inorganic anions play in MV salts of biferrocenium cations.[23] As shown in the powder neutron diffraction study of TbBaFe$_2$O$_5$ in ref 10, the direct iron to iron interactions reverse sign from FM above T_V to antiferromagnetic (AFM) below T_V, and the charge-ordered TbBaFe^{II}Fe^{III}O$_5$ adopts the G-type AFM structure. The strong coupling between the magnetic structure and the charge ordering raises several questions. What is the significance in this change of the local magnetic interaction at the charge-ordering transition? To what extent does the FM coupling between pairs of iron atoms stabilize the valence-mixed phase? Can the magnetic and the charge-ordering transitions be uncoupled through changes in the radius of the rare-earth ion? It has previously been observed from synchrotron powder X-ray diffraction experiments that when going from R = Sm to Nd a change in the space-group symmetry of the charge-ordered state occurs.[11] This hints at the possibility that for larger rare-earth ions the Verwey transition could be intrinsically different than previously characterized for R = Tb & Y. To

(9) Lindén, J.; Karen, P.; Kjekshus, A.; Miettinen, J.; Pietari, T.; Karppinen, M. *Phys. Rev. B* **1999**, *60*, 15 251.
(10) Karen, P.; Woodward, P. M.; Lindén, J.; Vogt, T.; Studer, A.; Fisher, P. *Phys. Rev. B* **2001**, *64*, 214 405.
(11) Karen, P.; Woodward, P. M.; Santosh, P. N.; Vogt, T.; Stephens, P. W.; Pagola, S. *J. Solid State Chem.* **2002**, *167*, 480.
(12) Woodward, P. M.; Karen, P. *Inorg. Chem.* **2003**, *42*, 1121.
(13) Karen, P.; Woodward, P. M. *J. Mater. Chem.* **1999**, *9*, 789.
(14) Er-Rakho, L.; Michel, C.; Lacorre, P.; Raveau, B. *J. Solid State Chem.* **1988**, *73*, 531.
(15) Karen, P., Unpublished data.
(16) Jacob, M.; Hansen, S.; Sturefelt, S. *Microscopy, Microanalysis, Microstructures* **1990**, *1*, 319.
(17) Chapman, J. P.; Attfield, J. P.; Molgg, M.; Friend, C. M.; Beales, T. P. *Angew. Chem., Int. Ed. Engl.* **1996**, *35*, 2482.
(18) Zhou, W.; Lin, C. T.; Liang, W. Y. *Adv. Materials* **1993**, *5*, 735.
(19) Verwey, E. J. W.; Haayman, P. W.; Romeijn, F. C. *J. Chem. Phys.* **1947**, *15*, 181.
(20) Wright J. P.; Attfield J. P.; Radaelli P. G. *Phys. Rev. Lett.* **2001**, *87*, 266 401.
(21) Robin, M. B.; Day, P. *Adv. Inorg. Chem. Radiochem.* **1967**, *10*, 247.
(22) Kakol, Z. *J. Solid State Chem.* **1990**, *88*, 104.
(23) Varret, F.; Linares, J.; Boukheddaden, K. *Chem. Phys.* **1996**, *212*, 487.

Table 1. Syntheses Data for Bulk Neutron-Diffraction Samples

	T (°C)	mixing ratio V_{Ar}/V_{H_2}	log p_{O2} (bar)[b]	log p_{H_2O} (bar)[c]
$NdBaFe_2O_{4.991(2)}$[a]				
calcination	900	56	−16.0	−1.67
sintering	1040	16	−14.7	−1.68
equilibration	830	0	−20.8	−1.62
$HoBaFe_2O_{5.004(1)}$[a]				
calcination	870	65	−16.5	−1.70
sintering	1000	50[d]	−14.3	−1.67
equilibration	1000	12.1	−15.4	−1.62

[a] Oxygen content as determined by cerimetric analysis. [b] Calculated. [c] According to the temperature at which the gas was moisturized. [d] It would have been more appropriate to decrease this value closer to that used for equilibration.

answer such questions, careful neutron diffraction studies as a function of temperature are essential. In this study, the evolution of both the crystal and magnetic structures of two members of $RBaFe_2O_5$ system are studied by powder neutron diffraction from 2 K through the Néel temperature. One variant, $HoBaFe_2O_5$, is based on the smallest R atom found to stabilize the double-cell perovskite type,[15] the other contains the largest R atom that can be incorporated before the oxygen vacancy and cation ordering are lost, viz., R = Nd. Both compounds are carefully synthesized as bulk samples with oxygen contents very close to the ideal intermediate valence state +2.5 of the iron atoms.

Experimental Section

Syntheses. Liquid-mixing technique via amorphous citrate precursors was adopted for syntheses. The rare-earth oxide (12.2511 g of Nd_2O_3, Molycorp, or alternatively 13.8169 g of Ho_2O_3, Stanford Materials, both >99.9%), standardized by annealing, was dissolved in 250 g of melted citric acid monohydrate (Fluka, < 0.02% ash as sulfate). A stoichiometric amount of iron (99.95%, lumps, Koch−Light) was converted to nitrate, diluted to 100 mL and added into the melt under an efficient magnetic stirring. After the nitrate groups had been largely removed in the form of nitrous gases upon continued warming, the melt was cooled below 100 °C and half of its volume of distilled water was added to facilitate the subsequent dissolution of $BaCO_3$ (0.1% Sr, Merck). The resulting clear viscous solution of an orange-brown color was transferred into a porcelain bowl and dehydrated at 180 °C in an drying oven into a dark-brown porous solid, milled, and slowly incinerated in a porcelain crucible with a lid over 5 days at 390 °C. After homogenization in a vibration agate mill, the X-ray amorphous precursor was calcined in a flowing atmosphere with a defined partial pressure of oxygen, homogenized, pressed into pellets of diameter 8 mm and fired in a defined flowing atmosphere under conditions to produce compact, practically fully sintered cylinders of black color with silvery luster. An approximately 10-g batch of the sample (several pellets) was then equilibrated for 5 d in a flowing atmosphere of a composition that stabilizes the desired sample stoichiometry, followed by quenching inside the closed system by a free fall into a metal cup filled with an atmosphere of high-purity argon (5 N, < 2 ppm O_2, dried upon passing through P_2O_5). A thin surface layer was removed from the cylinders before homogenizations for powder diffraction. An overview of the synthesis conditions is given in Table 1.

Oxygen Content Analyses. The oxygen content was determined by cerimetric titration of divalent iron formed after digesting the oxide in an ampule sealed under argon. Digestions of typically 0.2 g of the finely powdered sample in 5 mL of water and 4 mL of concentrated HCl lasted less than one minute at a temperature of approximately 60 °C. After complexation of the trivalent iron with some 10 mL of 50% phosphoric acid, the same amount of concentrated HCl was added, and the solution was titrated under argon atmosphere with 0.1 M solution of cerium(IV) sulfate at room temperature with ferroin as an indicator.

Differential Scanning Calorimetry (DSC). Determinations of temperatures of the premonitory and main Verwey transitions were performed with the help of a liquid-nitrogen operated Perkin−Elmer Pyris 1 instrument. Thermal-flux curves were registered between 170 and 340 K upon heating the samples in aluminum pans at a rate of 10 K/min. Peak temperatures were corrected to the zero sample-weight, based on a separate calibration series. The temperature scale was calibrated on cyclopentane, cyclohexane, *n*-octane, *n*-decane, *n*-dodecane, *m*-nitrotoluene, and *p*-nitrotoluene standards of >99.7% purity. The enthalpic effect was calibrated on low-temperature phase transitions of high-purity cyclohexane.

Synchrotron X-ray Powder Diffraction (SXPD). Data for determination of the molar volume of $HoBaFe_2O_5$ as a function of temperature were collected at the two-circle powder diffractometer equipped with helium-operated cryostat, installed at the BM1B beamline of ESRF in Grenoble. Argon-sealed sample in a glass capillary of 0.25 mm in diameter was rotated in the X-ray beam of wavelength λ = 0.48572 Å calibrated on NIST standard silicon. The reflection intensity from a 111-oriented silicon crystal analyzer was registered with a NaI scintillation counter. Short isothermal scans were performed between 100 and 350 K over the narrow angular range about the 200, 020, 004 Bragg reflections of the double-cell perovskite type. The d-values were obtained as Lorentzian peak maxima by least-squares fitting. SXPD data for $NdBaFe_2O_5$ are given in detail in ref 11.

Neutron Powder Diffraction (NPD). Diffraction patterns were obtained on two-axis diffractometers at the D2B and D20 beamlines of the reactor at the Institute Laue Langevin, located in Grenoble, France. High-resolution data (D2B) were collected between 0 and 150° (2θ) in the ILL cryofurnace using monochromatic radiation (Ge crystal, *hkl* 335) of the wavelength 1.59324(2) Å as calibrated on the CeO_2 NIST standard. The accuracy of the calibration is estimated to be about ±0.0002 Å, and the stability over the period of the data collections a further degree of magnitude lower. A divergence of 10′ at the collimator and a slit size of 10 mm ensured the highest resolution for the $NdBaFe_2O_5$ pattern collected over 12 h at 2 K (exhibiting a Nd magnetic order, vide infra), whereas a 30-mm slit size was used for other temperatures and for all $HoBaFe_2O_5$ patterns. An upper limit of approximately 10^5 counts per step of 0.05° (2θ) was maintained for all data collections. The samples were loaded into vanadium containers in a glovebag filled with He and then placed in the high (He) vacuum of the cryofurnace, preventing any possibility for oxidation.

Neutron Thermodiffractometry. High-intensity data (D20) for $NdBaFe_2O_5$ were collected between 10 and 140° (2θ) under a continuous temperature increase; first in the ILL vanadium cryostat (from 2 to 315 K, at a ramp of 0.3 K/min, scan time 4 min) and then in the ILL vacuum furnace with vanadium heating elements (from 300 to 473 K, at a ramp of 0.2 K/min, scan time 6 min). All data for $HoBaFe_2O_5$ were collected with a ramp of 1 K/min and a scan time of 2 min per data set. A wavelength estimate was made by fixing the D2B-derived unit-cell parameters in a simultaneous refinement of the D20 and D2B patterns (at 2 K) of $HoBaFe_2O_5$, giving λ = 2.40779 Å. The recorded sample temperatures during the cryostat run were calibrated linearly using two fixed end points: (1) The starting temperature of the sample, 2 K, which was assumed identical with the nominal value of 2 K, given the initial temperature equilibration. (2) Temperature of the structural effect of the Verwey transition for $HoBaFe_2O_5$ (302.5 K versus the correct value of 295 K from DSC runs; analogous values for $NdBaFe_2O_5$ were 220 and 215 K, respectively). Temperature readings from the furnace were not calibrated.

Rietveld Refinement Procedures. The GSAS program suite[24] was used for refinements of the D2B diffraction data. The pseudo-Voigt function #3 of GSAS was adopted to model the Bragg reflection profiles and the background was modeled using an 8-coeffient Chebyshev

(24) Larson, A. C.; Von Dreele, R. B. General Structure Analysis System (GSAS) Los Alamos National Laboratory Report LAUR 86-748 2000.

polynomial function. Peak-asymmetry model took into account the sample and detector height as well as the sample central displacement.[25] The peak asymmetry occurring due to a distribution of the oxygen contents[26] and hence unit-cell dimensions across the sample was not specifically modeled, but may have entered into the asymmetry correction. The Fullprof program[27] was used for the cyclic refinement of about 300 neutron thermodiffractometry patterns for each sample. The overall temperature range for a sample was separated into individual intervals for each occurring magnetic and nuclear symmetry type, and a correct overlap of these intervals was ensured by refining the border ranges with both models (viz., those below and above the particular structural change). Owing to the large asymmetry of the D20 Bragg profiles, the original D20 neutron wavelength estimate (by the combined refinement with GSAS) did not completely satisfy an agreement between the SXPD data and the cyclic refinement results by Fullprof. The refined D20 unit-cell parameters were therefore multiplied by a correction factor of 1.00115 that relates the 300 K D20 data with the SXPD results for $HoBaFe_2O_{5.000}$ at the same temperature.

Results

Localization of the Phase Transitions. On the basis of previous studies, three phase transitions are expected upon increasing temperature: (i) the main Verwey transition where the charge-ordered class-I MV state "melts" into the class-II MV state, (ii) the premonitory transition from a class-II MV state to a class-III MV state, and (iii) the Néel transition from the AFM state to a paramagnetic state. Figure 2 shows the DSC traces for $NdBaFe_2O_5$ and $HoBaFe_2O_5$. The large peaks mark the main Verwey transition (MV class I−II), at 295 and 215 K for R = Ho and Nd respectively, whereas the smaller peaks at 324 and 286 K correspond to the premonitory transition (MV class II−III). The difference in size between the large and small peaks reflects the different extent of the charge separation and ordering.[10] The difference in the magnitude and position of the strong peaks for R = Nd and Ho shows the influence exercised by the changing size of the R atom over the Verwey transition. Note that the DSC measurements do not cover the temperature range where the Néel transition into the paramagnetic state occurs.

Nuclear Crystal Structures above the Verwey Transition. At each temperature of the data collection in this region, viz., 240, 300, 375, and 450 K for $NdBaFe_2O_5$, and 340 and 450 K for $HoBaFe_2O_5$, both compounds were found isotypical with the class-III MV structure of $TbBaFe_2O_5$ [10] (Figure 1). The Rietveld refinements of the crystal structure were performed within the symmetry of the space group *Pmmm* of the prototype structure at all temperatures for sake of consistency. Tetragonal models were investigated for refinements of the 450 K data, giving a slightly poorer fit to the data for both compounds. It should be noted that very weak, broad magnetic peaks were present in the 450 K data sets indicating residual AFM fluctuations. It is expected that once the paramagnetism is fully established throughout the sample each crystallite will possess *P*4/*mmm* symmetry. The possible presence of a partial disorder between R and Ba was investigated during the course of the refinements, and no evidence was found to suggest that any deviations from complete cation order exist in either compound. The refined data show that above the main Verwey (MV class I−II) transition the crystal structures of both compounds are very similar. Unlike stoichiometric AMO_3 perovskites, where changes in the size of the A-site cation lead to significant changes in the M−O−M bond angles, the Fe−O distances and Fe−O−Fe angles are relatively insensitive to variations in the size of R. Besides the obvious change in the lattice parameters, the most significant impact of replacing the smaller Ho with Nd is an increase of ∼0.13 Å in the Fe−Fe distance (at 450 K) across the rare-earth layer. As this distance is rather long to begin with, one might assume that the physical properties would be relatively insensitive to such a change. However, as will be shown later, this seemingly innocuous structural modification has an impact on magnetic interactions under the transition. The results (see Supporting Information) also show a smooth structural progression throughout the temperature range of MV classes II and III, between T_V and T_N. In $NdBaFe_2O_5$ the 240 K data set falls clearly into the class-II range, viz., between the premonitory transition temperature, T_{PM}, and T_V. This data set was analyzed using both the valence-mixed model, where all iron atoms are crystallographically equivalent, and a charge-ordered model, where two crystallographically distinct iron atoms are present. The use of the more complicated charge-ordered model gave no improvement in the fit to the experimental data. Therefore, we must conclude that even though it is possible to observe two different Fe signals in the Mössbauer spectrum, a *long-range* three-dimensional charge order is not proven for the MV class-II phase.

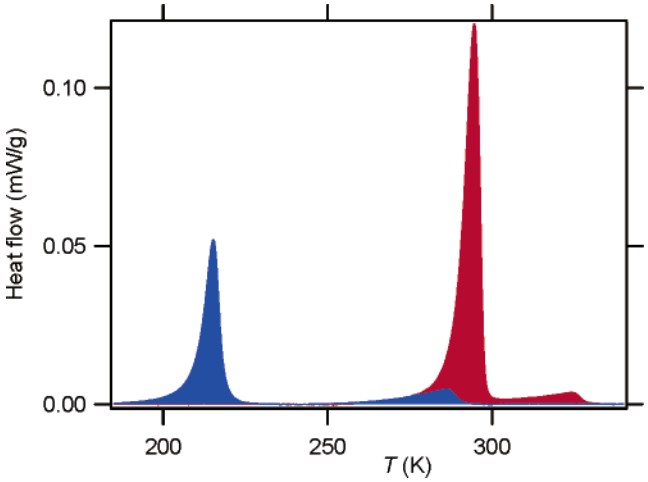

Figure 2. DSC peaks for $NdBaFe_2O_5$ (blue) and $HoBaFe_2O_5$ (red) upon heating. Areas give latent heat (ΔH) of the charge-ice melting.

Table 2. Rietveld-Refinements for $R BaFe_2O_5$ at 2 K

R	Nd	Ho
R_{wp}	0.0585	0.0505
R_p	0.0443	0.0390
$R(F^2)$	0.0442	0.0389
N_{obs}	1364	808
N_{var}	55	37
space group	$P2_1ma$	$Pmma$
a (Å)	7.9995(1)	8.03183(8)
b (Å)	3.91588(5)	3.83589(3)
c (Å)	7.6334(1)	7.52198(9)
volume (Å^3)	239.117(8)	231.746(4)

Nuclear Crystal Structures below the Verwey Transition. Table 2 gives an overview of the Rietveld refinement results at 2 K, with full crystallographic coordinates of the charge-ordered structure given in Table 3 for R = Ho, and Table 4 for R =

(25) Finger, L. W.; Cox, D. E.; Jephcoat, A. P. *J. Appl. Crystallogr.* **1994**, *27*, 892.
(26) Karen, P. *J. Solid State Chem.* **2003**, *170*, 9.
(27) Rodríguez-Carvajal, J. program Fullprof.2k, Version 2.10, March 2002.

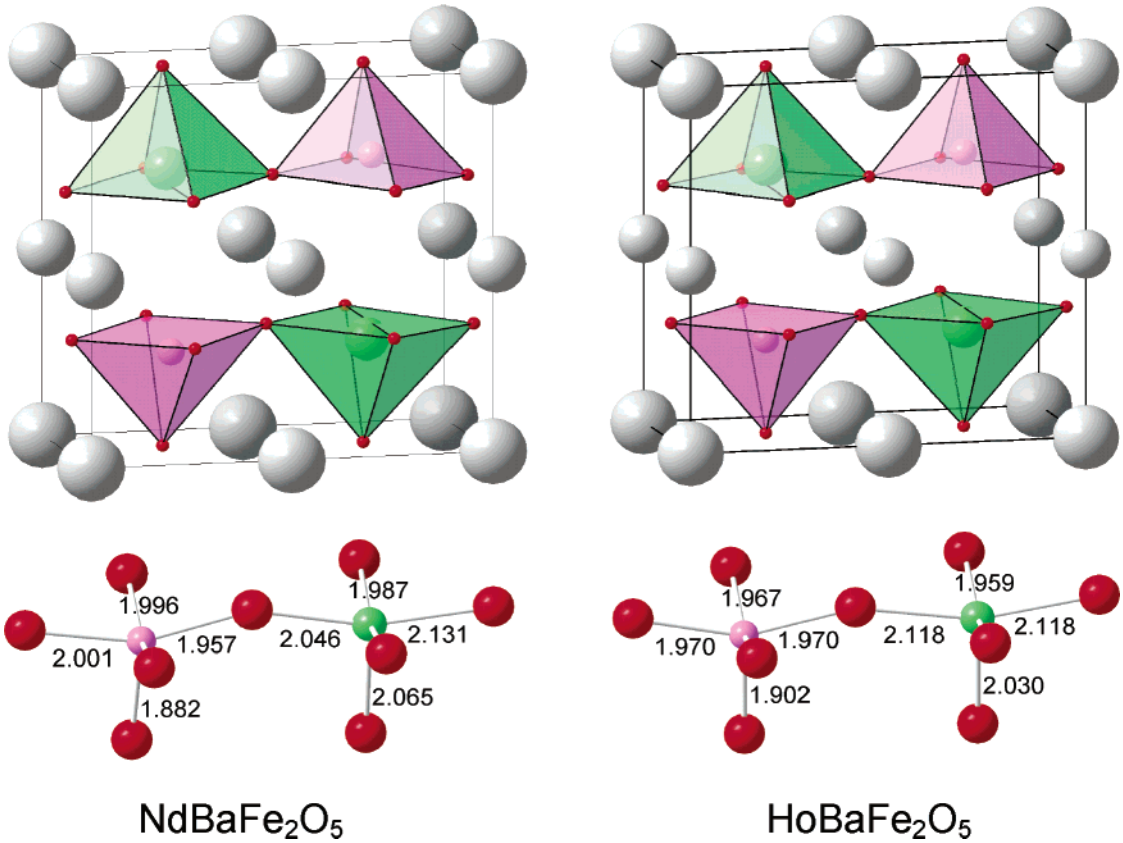

Figure 3. Charge ordering in $NdBaFe_2O_5$ ($P2_1ma$) and $HoBaFe_2O_5$ (*Pmma*). Divalent iron in green, trivalent in violet, internuclear distances in Å.

Table 3. Crystallographic Coordinates and Displacement Parameters for $HoBaFe_2O_5$ at 2 K[a]

atom	Wyckoff site	*x*	*y*	*z*	U_{iso} (Å^2)
Ba	2a	0	0	0	0.0030(5)
Ho	2c	0	0	1/2	−0.0004(3)
Fe(1)	2f	1/4	1/2	0.2548(4)	0.0027(2)[b]
Fe(2)	2f	3/4	1/2	0.2679(4)	0.0027(2)[b]
O(1)	2f	1/4	1/2	0.002(1)	0.0060(1)
O(2a)	2e	3/4	0	0.3210(7)	0.0038(3)[b]
O(2b)	2e	1/4	0	0.3128(7)	0.0038(3)[b]
O(3)	4j	0.0105(5)	1/2	0.3115(2)	0.0050(4)

[a] Unit cell information, space group and refinement statistics are given in Table 2. [b] The isotropic displacement parameters for Fe(1) and Fe(2) were constrained to be equal, as were the displacement parameters for O(2a) and O(2b).

Table 4. Crystallographic Coordinates and Displacement Parameters for $NdBaFe_2O_5$ at 2 K[a]

atom	Wyckoff site	*x*	*y*	*z*	U_{iso} (Å^2)
Ba	2a	0	0	0.001(1)	0.0027(5)
Nd	2a	0.009(1)	0	0.4941(7)	0.0009(4)
Fe(1)	2b	0.260(2)	1/2	0.2518(4)	0.0026(3)[b]
Fe(2)	2b	0.748(2)	1/2	0.2642(4)	0.0026(3)[b]
O(1)	2b	0.239(2)	1/2	0.0064(9)	0.0040(6)
O(2a)	2a	0.755(2)	0	0.3082(9)	0.0041(4)[b]
O(2b)	2a	0.259(2)	0	0.3025(9)	0.0041(4)[b]
O(3a)	2b	0.013(1)	1/2	0.2931(6)	0.0052(5)[b]
O(3b)	2b	0.498(1)	1/2	0.3155(6)	0.0052(5)[b]

[a] Unit-cell information, space group and refinement statistics are given in Table 2. [b] The isotropic displacement parameters for Fe(1) and Fe(2); O(2a) and O(2b); as well as O(3a) and O(3b) were constrained to be equal.

Table 5. Bond Distances (in Å) and Bond-Valence Sums for Charge-Ordered $HoBaFe_2O_5$ at 2 K

atom	Ho	Ba	Fe(1)	Fe(2)	BVS
O(1)		4×2.7768(0)	1.902(11)	2.030(11)	2.19(3)
O(2a)	2×2.418(3)	2×3.140(4)		2×1.959(2)	1.98(1)
O(2b)	2×2.453(3)	2×3.093(4)	2×1.967(2)		1.99(1)
O(3)	4×2.387(1)	4×3.029(1)	2×1.970(3)	2×2.118(3)	1.94(1)
BVS	2.81(1)	2.02(1)	2.95(3)	2.25(2)	

Note: Standard deviations in brackets are based on estimated errors of refined structural parameters.

Nd. For other temperatures within the charge-ordered states, the reader is referred to the Supporting Information.

The onset of charge ordering in $HoBaFe_2O_5$ leads to a doubling of the *a*-axis of the unit cell, and a change of symmetry from *Pmmm* to *Pmma*. This provides a unit cell with two crystallographically distinct sites for Fe. Bond distances and the bond-valence sums (BVS) are listed in Table 5 for $HoBaFe_2O_5$. The iron BVS show clearly that Fe(2) corresponds to divalent iron, whereas Fe(1) corresponds to trivalent iron. Significant elongation of the Fe(2)−O(3) bonds and the axial Fe(2)−O(1) bond leads to an asymmetric expansion of the $Fe^{2+}O_5$ square pyramids, whereas the $Fe^{3+}O_5$ square pyramids remain fairly symmetric. The shapes of the two square pyramids are shown in Figure 3. The charge-ordered structure of $HoBaFe_2O_5$ is analogous to the charge ordering previously observed in $TbBaFe_2O_5$ [10] and $YBaFe_2O_5$.[12] Molecular orbital (extended Hückel) calculations based on the charge-ordered structure of the latter compound show that the coordination environment about Fe^{3+} leads to a crystal-field splitting where the three lowest energy d-orbitals, d_{xy}, d_{xz}, and d_{yz}, are practically degenerate.[12] Such an environment is expected for the spherically symmetric high-spin d^5 ion. In contrast, elongation of the Fe^{2+}−O bonds directed along the *x*- and *z*-directions lowers

Table 6. Bond Distances (in Å) and Bond-Valence Sums for Charge-Ordered $NdBaFe_2O_5$ at 2 K

atom	Nd	Ba	Fe(1)	Fe(2)	BVS
O(1)		2×2.737(11)	1.881(13)	2.067(11)	2.14(7)
		2×2.863(11)			
O(2a)	2.478(27)	3.056(1)		2×1.987(3)	1.99(6)
	2.480(26)	3.120(1)			
O(2b)	2.478(12)	3.097(21)	2×1.996(2)		2.01(4)
	2.532(12)	3.014(21)			
O(3a)	2×2.488(6)	2×2.969(9)	2.001(23)	2.131(25)	1.91(7)
O(3b)	2×2.440(5)	2×3.110(10)	1.965(25)	2.038(22)	2.06(8)
BVS	3.02(10)	2.02(6)	2.87(10)	2.20(7)	

Note: Standard deviations in brackets are based on estimated errors of refined structural parameters.

Table 7. Magnetic Structure Refinement Results for $HoBaFe_2O_5$

T (K)	2	250	340	450
magnetic cell[a]	$a \times 2b \times c$	$a \times 2b \times c$	$2a \times 2b \times 2c$	$2a \times 2b \times 2c$
Shubnikov group	$Pm'm'a'$	$Pm'm'a'$	$Pmm'm$	$Pmm'm$
Fe M_y (μ_B)[b]	3.83(2)	3.48(2)	2.76(2)	c

[a] With respect to the nuclear unit cell. [b] Parallel to the y-axis so that $M_x = M_z = 0$. [c] Practically zero.

the energy of the d_{xz} orbital of the divalent iron, with respect to the d_{xy} and d_{yz} orbitals, thereby stabilizing an electronic ground state where the d_{xz} orbital is the only one of the five d-orbitals to be doubly occupied. Hence, the distortion of the $Fe^{2+}O_5$ square pyramids and the expansion of the a-axis occur in order to accommodate the double-occupied Fe^{2+} d_{xz} orbitals in an ordered fashion. It is also possible to think of this effect as a cooperative Jahn−Teller distortion; however, it should be noted that such a large distortion is unusual for a high-spin d^6 ion in an oxide.

The topology of the charge-ordered structure of $NdBaFe_2O_5$ is the same as observed for R = Ho, Tb, Y, but the finer details of the structure are somewhat different. Previous structure refinements utilizing synchrotron X-ray powder diffraction data showed the charge-ordered structure to have $P2_1ma$ space-group symmetry rather than the $Pmma$ characteristic of the other members of the RBaFe$_2$O$_5$ family. However, the bond distances and angles that could be extracted from the X-ray data were not of the same precision as those that can be obtained from high-resolution NPD data. This study has rectified this shortcoming and the two structural modifications can now be compared on equal footing. This comparison is illustrated graphically in Figure 3. Bond distances and BVS values are listed in Table 6. Although it is not immediately obvious why the Nd variant adopts a less symmetric crystal structure, it would seem as though the Nd ion is too large for the ideal charge and orbital ordered arrangement favored by the $Fe_2O_5^{5-}$ framework. This mismatch leads to a distortion of the ideal RBaFe$_2$O$_5$ charge-ordered structure in order to reduce unfavorable lattice strains. On the basis of simple considerations, the reduction of symmetry should reduce the electrostatic stabilization of the charge-ordered state.

Magnetic Structure of $HoBaFe_2O_5$. The refinement results for $HoBaFe_2O_5$ are given in Table 7. The magnetic phase transitions that occur in $HoBaFe_2O_5$ are of the same type as those already reported for $TbBaFe_2O_5$ [10] and $YBaFe_2O_5$.[12] Below the Verwey (MV class I−II) transition, the G-type AFM structure is observed. In the G-type magnetic structure, each iron couples AFM to each of its six nearest iron neighbors. Five

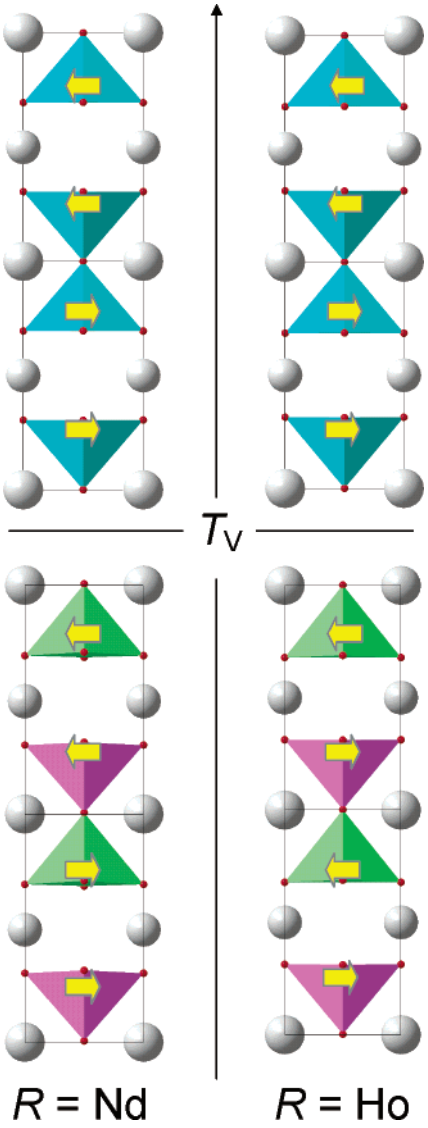

Figure 4. Magnetic coupling along c in RBaFe$_2$O$_5$ above and below the main Verwey transition temperature T_V. Divalent iron in green, trivalent in violet.

of these interactions are Fe−O−Fe superexchange interactions within the same square pyramidal double layer, whereas the sixth interaction is a direct Fe−Fe interaction across the rare-earth layer. Considering the electron configurations of high spin Fe^{2+} and Fe^{3+}, both of which give rise to a 1/2 filled d_{z2} orbital, AFM Fe−Fe coupling is expected. However, due to the relatively large Fe−Fe distance this coupling is expected to be much weaker than the oxygen mediated superexchange coupling. Interestingly, these interactions are the only ones that change at the Verwey transition (see Figure 4).

The alert reader will note that the moments of the Fe^{2+} and Fe^{3+} ions must necessarily be different in the charge-ordered state. Refinements were attempted using a model where the moments of these two ions were refined independently. Unfortunately, even though the average moment could be refined to a very accurate and reproducible value, the individual Fe^{2+} and Fe^{3+} moments were highly correlated, which led to very large uncertainties in their values. This effect was problematic in refinements of both the D2B data and the D20 data, as well as in combined refinements. Therefore, we elected to analyze the

Table 8. Magnetic Structure Refinement Results for $NdBaFe_2O_5$

T (K)	2	175	240	300	375	450
magnetic cell[a]	$a \times 2b \times 2c$	$a \times 2b \times 2c$	$2a \times 2b \times 2c$	$2a \times 2b \times 2c$	$2a \times 2b \times 2c$	$2a \times 2b \times 2c$
Shubnikov group	$P2_1m'a'$	$P2_1m'a'$	$Pmm'm$	$Pmm'm$	$Pmm'm$	$Pmm'm$
Fe M_y (μ_B)[b]	3.83(2)	3.69(2)	3.44(2)	3.13(2)	2.53(2)	1.13(2)
Nd M_x (μ_B)[c]	1.13(4)					

[a] With respect to the nuclear unit cell. [b] Parallel to the y-axis so that $M_x = M_z = 0$. [c] Parallel to the x-axis so that $M_y = M_z = 0$.

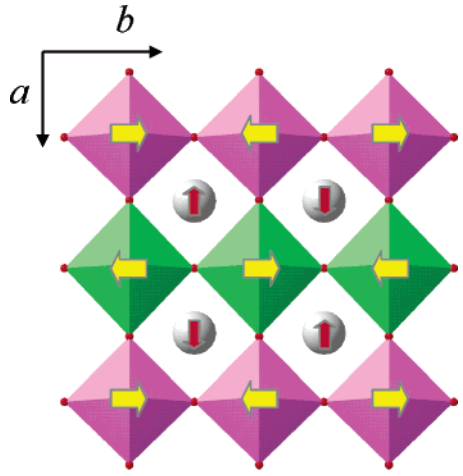

Figure 5. Magnetic structure at 2 K of $NdBaFe_2O_5$: Section of the *ab* plane showing one Nd layer and a single layer of iron square pyramids above it.

data using a single average moment for the two iron sites. A similar effect was previously noted in $YBaFe_2O_5$.[12]

Magnetic Structure of $NdBaFe_2O_5$. The magnetic structure refinement results for $NdBaFe_2O_5$ are given in Table 8. The magnetic phase transitions that occur in $NdBaFe_2O_5$ are distinctly different in two ways from those observed in other RBaFe$_2$O$_5$ compositions (see Figures 4 and 5). First of all, the Verwey (MV class I−II) transition does not trigger a rearrangement of the magnetic structure. Consequently, the room-temperature-$YBaFeCuO_5$-type[28] AFM structure is observed both above and below T_V. It is quite probable that this unexpected difference originates from a reduction in the strength of the direct Fe−Fe magnetic interaction due to the increased Fe−Fe distance of the Nd structure. Apparently as this interaction becomes exceedingly weak the driving force for reorienting the spins at T_V becomes insufficient to trigger the transition. Second, a G-type AFM ordering of the Nd ions is observed at 2 K (Figure 5), whereas no ordering of Ho ions was detected.

Neutron Thermodiffractometry. Although the DSC measurements are very useful for detecting and characterizing thermodynamic aspects of phase transitions, they do not provide any details regarding changes in the crystal and/or magnetic structure. Conversely, high-resolution NPD measurements give detailed structural information, but the long data collection times necessitate a very coarse grid of temperature points, making it difficult to detect subtle changes and accurately determine transition temperatures. Fortunately, recent advances in instrumentation (primarily detectors) have made it possible at a few facilities throughout the world to collect high quality NPD data sets on time scales varying from a few minutes to microseconds. This allows data sets to be collected on a temperature grid and time scale that are comparable to thermal analysis methods. This technique, sometimes referred to as neutron thermodiffractometry, provides information that is highly complementary to the thermodynamic data obtained from DSC measurements and the structural snapshots obtained using high-resolution NPD methods. To fully characterize the phase transitions in the RBaFe$_2$O$_5$ system, we carried out thermodiffractometry experiments on $HoBaFe_2O_5$ and $NdBaFe_2O_5$ through all three phase transitions, using the D20 diffractometer at the ILL. Figure 6 shows the evolution of NPD patterns as a function of temperature for both compounds. The appearance of the steep rise in the intensity at about 26.5°, 37.4°, 53.5°, and 57.9° 2θ, below some 450 K in both compounds, indicates the onset of the $YBaFeCuO_5$-type AFM ordering. Any changes that accompany the premonitory charge-ordering transition are too subtle to see in these plots, an observation that is not unexpected from previous investigations. However, at the main charge-ordering (Verwey) transition the diffraction patterns change significantly. A pronounced increase in peak splitting is observed in the diffraction patterns collected below T_V in both compounds, revealing a large increase in the orthorhombic distortion of the unit cell. This distortion originates from orbital ordering in the low-temperature charge-ordered state. Although the structural behavior of the two compounds appears similar on the surface, it is easy to see that the magnetic structures of these two compounds respond differently to the onset of long-range charge ordering, confirming the D2B results. In $HoBaFe_2O_5$, the positions of the magnetic Bragg peaks change dramatically at the Verwey transition, consistent with a change in the magnetic structure to the G-type AFM. On the other hand, the evolution of the magnetic Bragg peaks in $NdBaFe_2O_5$ reveals that the magnetic structure undergoes little change in response to charge ordering. To better quantify the information obtained from the thermodiffractometry experiments, Rietveld refinements were carried out in order to extract the evolution of the unit cell parameters and magnetic moments as a function of temperature. Due to the limited range of q-space that is contained in these diffraction patterns unconstrained Rietveld refinements were not feasible. Therefore, the atomic coordinates and displacement parameters were fixed at values derived from the high-resolution D2B refinements for each particular nuclear- and magnetic-symmetry phase, whereas the unit-cell parameters, peak-shape parameters, magnetic moments and an overall temperature factor were freely refined.

Neutron Thermodiffractometry; Magnetic-Moment Evolution. Figure 7 shows the evolution of the refined ordered magnetic moments on Fe and Nd. Because there is no change in the arrangement of the AFM moments in $NdBaFe_2O_5$, the ordered iron magnetic moment proceeds almost smoothly through the Verwey (MV class I−II) transition, showing only a minute increase. In $HoBaFe_2O_5$, a dramatic rearrangement of the spins occurs, resulting in a magnetic disorder within the transition range owing to onset of critical behavior in the vicinity of T_V across the sample. Except for this, both compounds have practically the same magnitude of the ordered magnetic moment, and the practically equal Néel temperatures suggest that the stability of antiferromagnetism in the valence-mixed phase is

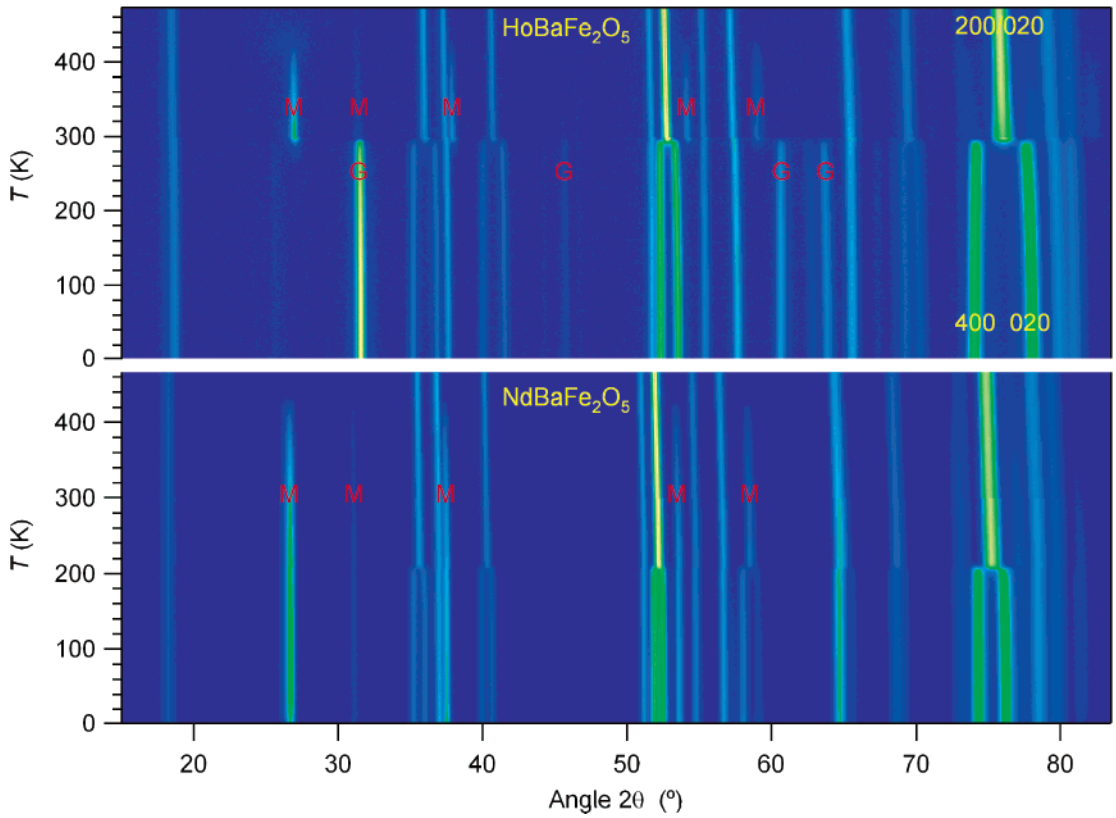

Figure 6. Bragg-peak altitude plot from neutron thermodiffractometry of $HoBaFe_2O_5$ and $NdBaFe_2O_5$. Symbols M and G identify the main peaks of the $YBaFeCuO_5$ and G magnetic-structure types, respectively.

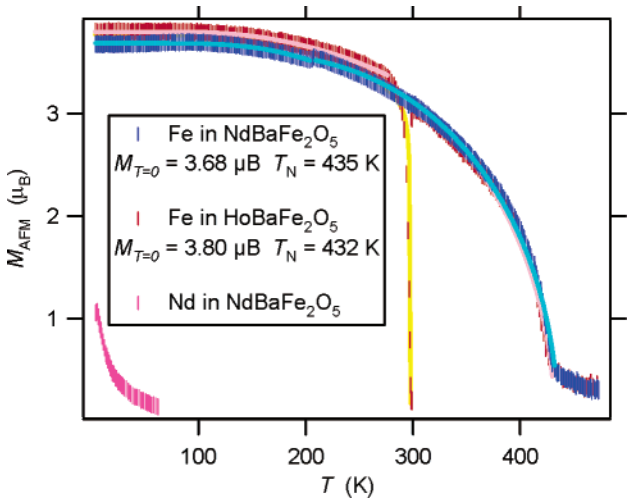

Figure 7. Temperature evolution of the refined AFM moments in $NdBaFe_2O_5$ (of iron in blue, of neodymium in violet) and $HoBaFe_2O_5$ (of iron, in red). Brillouin fits in related lighter colors give moments at zero temperature (the $T < T_V$ range) and Néel temperatures (the $T > T_V$ range) listed in the legend. Critical behavior at Verwey (MV class I−II) transition for iron moment in $HoBaFe_2O_5$ is fitted by a $(T_V - T)^{-\gamma}$-type function (in yellow); but must be considered a guide for eye because also an oxygen nonstoichiometry distribution contributes to the width of the critical region.

rather insensitive to changes in the radius of *R* and the Fe−Fe distance. As apparent from the Brillouin fits (for details on the procedure see ref 10), the temperature evolution of the ordered magnetic moments below and above T_V is somewhat different, and the ordered magnetic moments at absolute zero and the Néel temperatures are therefore evaluated separately from these two temperature ranges. The curvature below T_V corresponds to the parameter *J* (total angular-momentum quantum number) being approximately 1.5, suggesting that the orbital angular momentum is not quenched in the charge-ordered state. This may well be the case as the doubly occupied orbital of Fe^{2+} is calculated[12] energetically rather close to the other two t_{2g} orbitals. On the other hand, the steep fall of the curve in the valence-mixed state (above T_V) gives $J = 0$, suggesting no spin−orbit interactions in the valence-mixed state. The AFM moments at low temperature are somewhat lower than might be expected for a combination of high-spin Fe^{2+} and Fe^{3+} ($\sim$4.5 μ_B), but not unreasonably low. Previous Mössbauer measurements confirm the high-spin states of the two ions.[9]

The onset of the cooperative Nd magnetism occurs near 30 K and reaches a value of $\sim$1.1 μ_B at 2 K. These values are in rough agreement with Nd magnetic ordering in other perovskites, such as $NdCrO_3$ ($T_N = 12$ K, moment $= 1.9\ \mu_B$)[29] and $NdFeO_3$ ($T_N \cong 25$ K, moment $= 0.9\ \mu_B$).[30] The temperature evolution of the Nd moment does not exhibit the expected Brillouin functionality. Rather, the large concavity of the Nd moment vs temperature plot is reminiscent of the *R* magnetic moment evolution in $NdCrO_3$, $HoCrO_3$, and $ErCrO_3$, where the rare-earth magnetic ordering is induced by the magnetic ordering of the Cr^{3+} sublattice.[29] It is interesting to note that among $RCrO_3$ perovskites there is no clear indication that $NdMO_3$ phases have a stronger tendency toward *R*-spin ordering than their Ho counterparts.[29,31] However, the observation of induced magnetism in $NdBaFe_2O_5$ indicates that the *R* ordering is intimately tied to the Fe ordering. The contrasting magnetic

(28) Ruiz-Aragón, M. J.; Morán, E.; Amador, U.; Martínez, J. L.; Andersen, N. H.; Ehrenberg, H. *Phys. Rev. B* **1998**, *58*, 6291.
(29) Shamir, N.; Shaked, H.; Shtrikman, S. *Phys. Rev. B* **1981**, *24*, 6642.

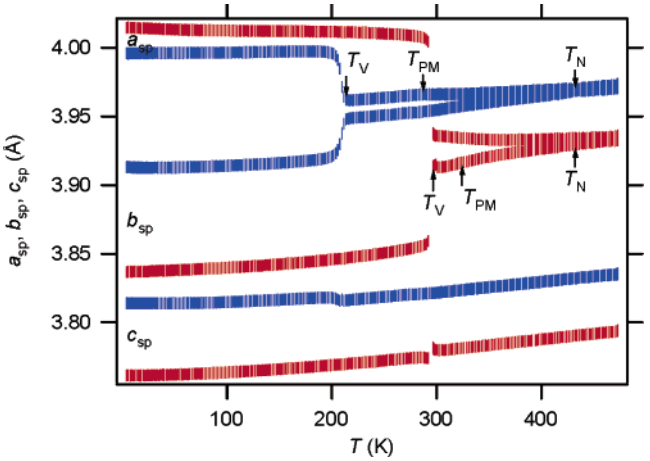

Figure 8. Temperature evolution of the single-perovskite-type cell parameters (a_{sp}, b_{sp}, and c_{sp}) for $RBaFe_2O_5$ (R = Nd in blue, Ho in red). Positions of the AFM ordering, premonitory and main Verwey transitions are marked. Plot markers do not necessarily represent error bars.

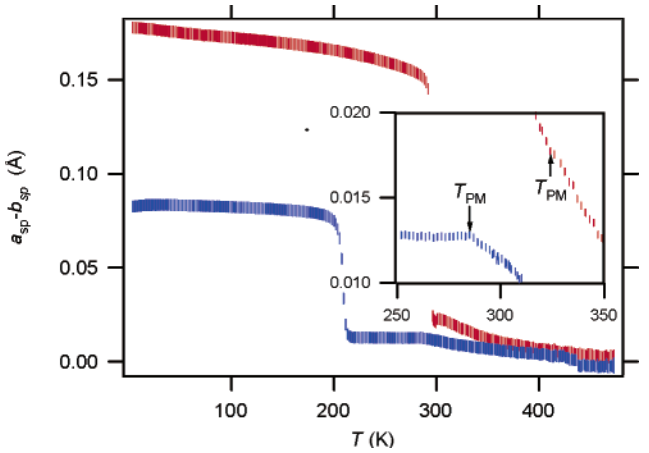

Figure 9. Temperature evolution of the orthorhombic distortion a_{sp}-b_{sp} in $RBaFe_2O_5$ (referring to a single-perovskite cell; R = Nd in blue, Ho in red). Positions of the premonitory charge-ordering transition are located in detail in the inset.

ordering of iron at low temperature is therefore most likely responsible for the different magnetic behavior of R = Nd and Ho.

Neutron Thermodiffractometry; Unit-Cell Evolution. Figure 8 shows the result for both compounds. This figure reveals that the onset of the orthorhombic distortion occurs at the Néel temperature in both compounds. The tetragonal to orthorhombic transition is linked to the onset of antiferromagnetism through a magnetostrictive effect, which originates from the fact that the Fe moments are directed parallel to the *b*-axis, thereby breaking the strict tetragonal symmetry. The magnitude of this distortion is shown more clearly in Figure 9, where the evolution of the orthorhombic distortion index ($a-b$) is plotted as a function of temperature. In both compounds, the distortion increases dramatically at the main charge-ordering transition, although the effect is more than twice as large in the R = Ho variant. The expanded region in the inset of Figure 9 reveals a structural signature of the premonitory charge-ordering transition in $NdBaFe_2O_5$. Namely, the size of the orthorhombic distortion index steadily increases between T_N and T_{PM}, and then remains constant between T_{PM} and T_V. Similar behavior is not observed at the premonitory transition in $HoBaFe_2O_5$.

Table 9. Thermodynamics of the Successive Valence-Mixing Transitions upon Heating $HoBaFe_2O_5$ (present paper) and $NdBaFe_2O_5$ (in italics, from ref 11, for easy comparison)

transition	MV class I–II	MV class II–III
T_V (in K; peak value)	295.7(10) *216(1)*	324.5(5) *286.3(3)*
ΔV ($Jbar^{-1}mol^{-1}$)	−0.0217(15) *−0.0235(6)*	not discernible
ΔH (kJ mol^{-1})	2.49(7) *1.07(4)*	0.180(15) *0.22(3)*
ΔS ($Jmol^{-1}K^{-1}$)	8.48(27) *5.00(1)*	0.56(4) *0.79(10)*
T_V (in K; peak-center value[a])	293(17) *214(14)*	319(51) *281(67)*
dP/dT_V ($barK^{-1}$)[b]	−386(39) *−211(4)*	not applicable

[a] As given by $T = \Delta H/\Delta S$. [b] From Clapeyron equation.

Thermodynamic Parameters of the Verwey Transitions in $HoBaFe_2O_5$. Table 9 compares the molar volume, enthalpies, and entropies for the valence-mixing transitions in $HoBaFe_2O_5$ with those obtained[11] for $NdBaFe_2O_5$. Thermal data for $HoBaFe_2O_5$ originate from DSC results for four samples with compositions in the interval $0.000 < w < 0.014$, for which the evaluated parameters were averaged. Volume data for $HoBaFe_2O_5$ originate from neutron thermodiffractometry and are compared in Figure 10 with the same results for $NdBaFe_2O_5$. In terms of the volume change at the transition, the data are fully consistent with those obtained by SXPD [$\Delta V/V = -0.00305(30)$ by SXPD for a $HoBaFe_2O_{5.000}$ sample versus −0.00308(10) obtained by thermodiffractometry for the $HoBaFe_2O_{5.004}$ sample].

With data collected upon heating, the signs of the derived parameters in Table 9 correspond to the analogy[26] with charge-ice melting. The entropy and enthalpy changes at the main Verwey (MV class I−II) transition are significantly higher than those observed for $NdBaFe_2O_5$, comparable with the values measured for R = Tb[10] and Dy[15] and smaller than those observed for R = Y.[12] In contrast, entropies and enthalpies of the premonitory (MV class II−III) transition change very little across the R series.

Discussion

In a periodic solid the stabilities of both the valence-mixed and charge-ordered states depend on cooperative interactions between valence states, electron spin orientation and orbital occupation. What makes $RBaFe_2O_5$ double-cell perovskites so special to transform through all three Day−Robin classes as a function of temperature? This can only occur owing to a fine balance between stabilities of the two limiting cases: class-III MV (valence-mixed) and class-I MV (charge-ordered). This study gives important clues regarding the relative factors that stabilize each state. Let us consider in turn how magnetic ordering and orbital ordering couple with the competing mixed-valence states, and how changes in the size of the R ion influence this coupling.

As stated earlier, the half occupancy of the Fe d_{z2} orbitals dictates that direct Fe−Fe exchange coupling in the charge-ordered state should be AFM, unless this interaction is so weak as to be of diminishing importance. On the other hand, it is possible that the valence-mixed state is stabilized by a double-exchange type interaction that allows carrier exchange across the R layer. If so, then the Fe−Fe coupling in the valence-mixed state should be FM. Experimentally, $HoBaFe_2O_5$ (as well as all

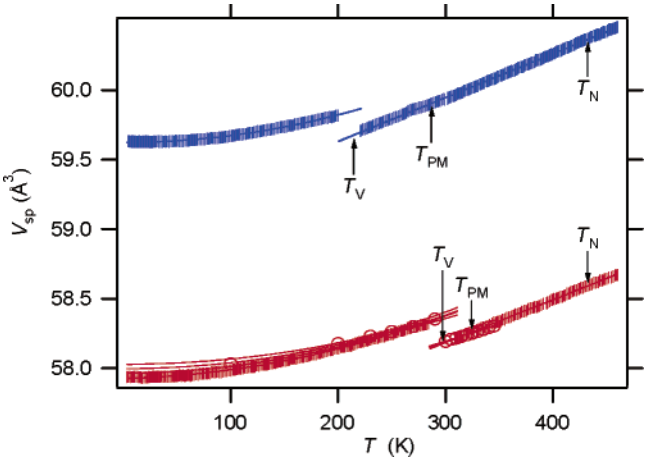

Figure 10. RBaFe$_2$O$_5$ volume (referring to a single-perovskite cell; R = Nd in blue, Ho in red) from neutron thermodiffractometry. A comparison with discrete SXPD data (circles).

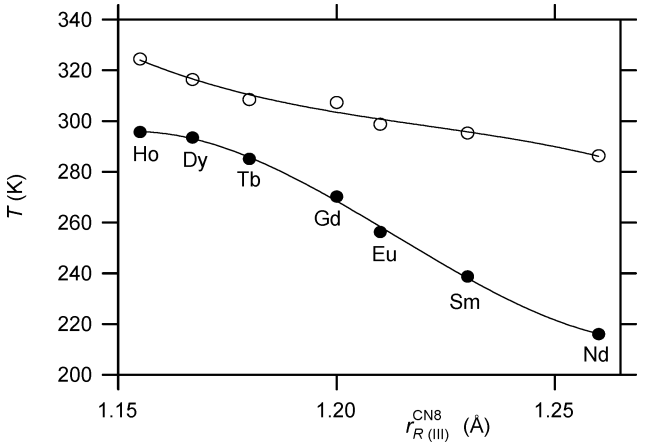

Figure 11. Temperatures of the premonitory (open circles) and main (full circles) charge-ordering transitions in RBaFe$_2$O$_5$ as a function of the Shannon R^{3+} ionic "crystal" radii[32] for CN = 8. References: 11 (Nd, Sm), 15 (Eu, Dy), 26 (Gd), and 9 (Tb).

previously studied RBaFe$_2$O$_5$ variants) indeed exhibits an FM Fe−Fe direct coupling in the valence-mixed state whereas an AFM Fe−Fe direct coupling in the charge-ordered state. Replacing Ho^{3+} with the larger Nd^{3+} increases the Fe−Fe separation and weakens the Fe−Fe direct exchange interaction. Interestingly, neither the magnetic order observed in the valence-mixed state nor the Néel temperature seems to be perturbed by this substitution. This would suggest that the Fe−Fe exchange interaction across the R layer does not play a significant role in stabilizing the valence-mixed state. This is not to say that the magnetic interactions are of no importance in the valence-mixed state. The magnetic ordering that occurs at ~435 K dictates the direction in which the crystal-structure is going to contract under all subsequent symmetry breakings. The magnetostrictive contraction along b induces the tiny orthorhombic distortion in which the intermediate, class-II state is formed by a partial disproportionation of the valence-mixed state upon cooling.

In contrast, the temperature of the main charge-ordering transition in RBaFe$_2$O$_5$ is affected by changing the rare-earth ion. Figure 11 shows a correlation of the transition temperatures with the R radius. It is seen that the relative stability of the charge-ordered state increases as the size of the rare-earth ion decreases. Yet the associated contraction of bond lengths should strengthen interactions pertinent to the valence-mixed state such as the double exchange behind the direct Fe−Fe FM coupling. However, what happens is quite the opposite, the charge-ordered arrangement becomes stronger and the charge-melting temperature increases. Suddenly, for R = Nd, the direct Fe−Fe FM coupling persists into the charge-ordered state without significantly deviating the trend in T_V as a function of the R ionic size. This coupling probably contributes somewhat to the relatively high electrical conductivity of the charge-ordered NdBaFe$_2$O$_5$ when compared with the other R variants,[11] considering that the RBaFe$_2$O$_5$ conduction is clearly not metallic.[10,11] The overall conjecture is that changing R does not affect *significantly* the stability of the valence-mixed state whereas it gradually changes the stability of the charge-ordered state. What is behind such an effect?

The structural charge-ordering pattern violates the simple electrostatic condition[33] for point-charge approximation that calls for charges alternating in all three directions. In and of itself this suggests participation of the orbital ordering, because the ground state can only be understood through consideration of a spatial charge distribution (as opposed to a point-charge distribution). The observed orthorhombic distortion identifies the d_{xz} Fe^{2+} orbital as the one being ordered, energy minimized and doubly occupied. How do the preconditions for such an orbital ordering change as a function of the R size? The difference in the lattice metrics, bond distances and bond valence sums (BVS) gives important clues about this. Note from Tables 5 and 6 that Ba has a rather unsymmetrical coordination environment, whereas R is highly symmetrical for both R = Nd and Ho variants. Furthermore, Ba has approximately the correct BVS, whereas both Nd and Ho are underbonded. This may be understood in terms of the contrast in polarizabilities of the Ba and R ions. The larger, softer Ba^{2+} ion is more easily deformable, leading to its unsymmetrical environment. However, the Ba−O(1) bonds are quite short, making them resistant to further compression. An elementary geometric consideration shows that the (average) Ba−O(1) distance is very sensitive to a net expansion or contraction in the *ab* plane, but rather insensitive to small orthorhombic distortions. This bulky yet soft ion hence dictates the volume, but not the distortion of the structure. The underbonded R ion is hard and does the opposite, it survives in a larger volume than it prefers, but controls the orthorhombic distortion. The consequence is that an increased size of R allows for less orthorhombic distortion hence less effective orbital ordering. This correlates with the observed decrease in T_V (as well as ΔH and ΔS) toward NdBaFe$_2$O$_5$.[10−12,26] Why then does the critical temperature of the premonitory charge-ordering transition decrease so little toward Nd, as seen from Figures 2 and 11? It is because this transition occurs within the magnetostrictive orthorhombic distortion that is approximately 10 times smaller than the subsequent distortion that accompanies a "complete" charge ordering. Thus, this transition from a class-III MV state to a class-II MV state is not highly coupled with the ease of orbital ordering. Even then, once the premonitory charge ordering is accomplished upon cooling, the lattice

(30) Bartolomé, J.; Palacios, E.; Kuzmin, M. D.; Bartolomé, F.; Sosnowska, I.; Przeniosło, R.; Sonntag, R.; Lukina, M. M. *Phys. Rev. B* **1997**, *55*, 11 432.
(31) Bhattacharjee, A.; Saito, K.; Sorai, M. *J. Phys. Chem. Solids* **2002**, *63*, 569.
(32) Shannon, R. D. *Acta Crystallogr. Ser. A* **1976**, *32*, 751.
(33) Anderson, P. W. *Phys. Rev.* **1956**, *102*, 1008.

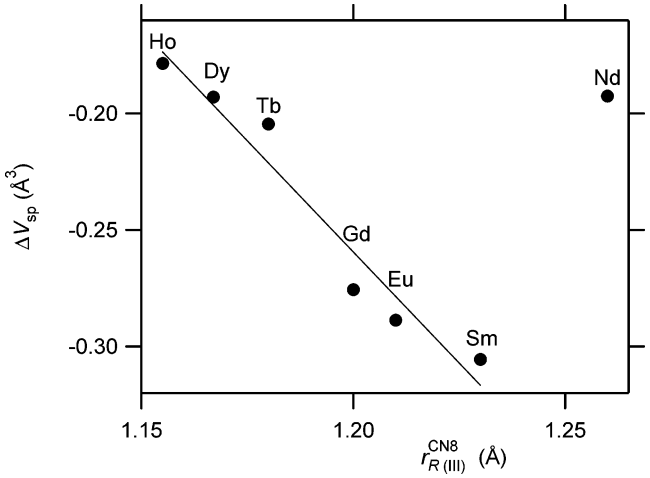

Figure 12. Volume changes ΔV at the main charge-ordering transition in $R BaFe_2O_5$ as a function of the Shannon R^{3+} ionic "crystal" radii[31] for CN = 8. References: 11 (Nd, Sm), 15 (Eu, Dy), 26 (Gd), and 9 (Tb).

deformation stops in $NdBaFe_2O_5$, whereas it is allowed to continue by the smaller Ho ion in $HoBaFe_2O_5$ (see Figure 9).

The thermal parameters of the main charge-ordering (Verwey) transition vary smoothly as a function of the R^{3+} radius. This begs the question which parameter is responsible for the sudden symmetry change for the charge-ordered structure of $NdBaFe_2O_5$, as compared with the other *R* variants. The answer is provided in Figure 12. It is the volume change ΔV at the transition that correlates with this discontinuity. Up to R = Sm, the volume difference increases, whereas the orbital ordering is being accommodated within the symmetry *Pmma*. For $NdBaFe_2O_5$, the projected ΔV becomes apparently too large, the symmetry changes to $P2_1ma$, and the increased deformation allows the charge ordering to proceed with a substantially diminished volume increase. The effectiveness of this trade off can be seen from a comparison of the smooth change in stability of the charge-ordered state (T_V as a function of the *R* radius in Figure 11) with the discontinuous evolution of ΔV in Figure 12. The latter result identifies again the orbital ordering as the underlying cause for the Verwey transition in $R BaFe_2O_5$. The d_{xz} orbital ordering of Fe^{2+} persists and continues, by slightly different means, even when the sterical conditions became unfavorable because of a too large "spectator" *R* atom. This makes a full circle to the premise of this discussion; we see again that it is the cooperative nature of the orbital ordering that dictates the important features of the charge-ordering transitions in $R BaFe_2O_5$.

Conclusions

Both end phases of the title double-cell perovskite series, $NdBaFe_2O_5$ and $HoBaFe_2O_5$, transform through all three Day−Robin classes of MV as a function of temperature. The phase transitions observed in $HoBaFe_2O_5$ are similar to those in previously studied compounds in the $R BaFe_2O_5$ family. Upon cooling, this sequence includes a paramagnetic to AFM transition within the class-III MV state (432 K), followed by a premonitory charge-ordering transition to a class-II MV state (324 K), followed by a more or less complete charge ordering to a class-I MV state (295 K). The onset of AFM ordering induces a magnetostrictive distortion of the unit cell, lowering the symmetry from tetragonal (*P*4/*mmm*) to orthorhombic (*Pmmm*). The transition into the fully charge-ordered state (*Pmma*) is accompanied by a reversal of the direct Fe−Fe magnetic exchange interactions and a dramatic increase in the magnitude of the orbital ordering. The latter is manifested in an orthorhombic distortion that minimizes the energy of the (doubly occupied) d_{xz} Fe^{2+} orbitals. Ordered stacking of these orbitals under formation of linear chains of Fe^{2+} explains violation of the electrostatic condition for ordering of point charges that otherwise would suggest a checkerboard pattern in all three dimensions. The charge-ordering transition in $NdBaFe_2O_5$ differs from the other studied $R BaFe_2O_5$ compounds in the following aspects: (1) the volume increase is about one-half of that expected from the trend between R = Ho and Sm; (2) the symmetry of the charge-ordered state is lowered from *Pmma* to $P2_1ma$; (3) the Fe−Fe magnetic interactions along *c* remain FM in the charge-ordered state; and (4) the size of the magnetostrictive distortion remains constant across the entire temperature range over which the class-II MV state is observed.

Yet the following parameters of the charge-ordering transition in $NdBaFe_2O_5$ fail to deviate significantly from the smooth function of the *R* ionic size: (1) the charge-ordering (Verwey) transition temperature; and (2) degree of the charge (orbital) ordering as measured by: (a) the orthorhombic distortion, (b) ΔH and ΔS, and, (c) the bond-valence sums at the two different iron atoms.

These observations suggest several conclusions. (1) A particular type of magnetic order does not *significantly* stabilize either the valence-mixed or charge-ordered states. (2) The main factor controlling conversions between the three Day−Robin MV classes in $R BaFe_2O_5$ is the stability of the charge-ordered state. (3) The stability of the charge-ordered state is controlled primarily by stereochemical conditions that allow for the ordering of the Fe^{2+} d_{xz} orbitals, which become doubly occupied. (4) Magnetic interactions decide the orientation but not the spatial pattern of the orbital ordering. (5) Minimization of the strain energy that accompanies the orbital ordering is of primary importance. This is achieved by structural means that may vary discontinuously across a structural series. This case study clearly demonstrates that charge-ordering transitions in $R BaFe_2O_5$ can only be understood through considerations of the cooperative interactions between orbital- and spin ordering in addition to electrostatic considerations.

Acknowledgment. Experimental assistance from the staff of the Swiss-Norwegian Beam Lines at ESRF is gratefully acknowledged. Patrick Woodward acknowledges the support of Ohio State University and the National Science Foundation (Grant No. DMR-0094271).

Supporting Information Available: (1) Crystallographic information files (CIF) for $NdBaFe_2O_5$ and $HoBaFe_2O_5$ at various temperatures. (2) Numerical data for temperature dependences of the refined unit-cell parameters and magnetic moments. (3) Tables of refined structural parameters of $NdBaFe_2O_5$ and $HoBaFe_2O_5$ at other temperatures than 2 K. This material is free of charge via the Internet at http://pubs.acs.org.

JA034813+